A PV-approach for dense water formation along fronts: Application to the Northwestern Mediterranean

Hervé Giordani, Cindy Lebeaupin Brossier, Fabien Léger, Guy Caniaux

RESEARCH ARTICLE

Special Section:

Dense Water Formations in the North Western Mediterranean: From the Physical Forcings to the Biogeochemical Consequences

Key Points:

- The mechanisms of dense water formation along the baroclinic gyre are investigated through a PV-budget
- Along the northern branch of the North Current, the surface frictional PV-flux drives a cross-front ageostrophic circulation
- The surface non-advective PV-flux involves energy exchanges down to -1400 W/m^2

Correspondence to:
H. Giordani,
herve.giordani@meteo.fr

A PV-approach for dense water formation along fronts: Application to the Northwestern Mediterranean

Hervé Giordani [ID][1], Cindy Lebeaupin-Brossier[1], Fabien Léger[1], and Guy Caniaux[1]

[1]Centre National de Recherches Météorologiques (CNRM-GAME) UMR 3589 (Météo-France/CNRS), Toulouse, Cedex 01, France

Abstract The mechanisms of dense water formation ($\sigma > 29.0$ kg m^{-3}) at work in the baroclinic cyclonic gyre of the North-Western Mediterranean basin are investigated through a PV-budget (PV: Potential Vorticity). The PV-budget is diagnosed from an eddy-resolving ($1/36°$) ocean simulation driven in surface by hourly air-sea fluxes provided by a nonhydrostatic atmospheric model at 2.5 km resolution. The PV-budget is controlled by the diabatic, frictional, and advective PV-fluxes. Around the gyre the surface diabatic PV-flux dominates the PV-destruction, except along the northern branch of the North Current where the surface frictional PV-flux is strongly negative. In this region, the bathymetry stabilizes the front and maintains the current northerly in the same direction as the dominant northerly wind. This configuration leads to optimal wind-current interactions and explains the preponderance of frictional PV-destruction on diabatic PV-destruction. This mechanical forcing drives a cross-front ageostrophic circulation which subducts surface low-PV waters destroyed by wind on the dense side of the front and obducts high-PV waters from the pycnocline on the light side of the front. The horizontal PV-advections associated with the geostrophic cyclonic gyre and turbulent entrainment at the pycnocline also contribute to the PV-refueling in the frontal region. The surface nonadvective PV-flux involves energy exchanges down to -1400 W m^{-2} in the frontal zone: this flux is 3.5 times stronger than atmospheric buoyancy flux. These energy exchanges quantify the coupling effects between the surface atmospheric forcing with the oceanic frontal structures at submesoscale.

1. Introduction

The North-Western Mediterranean is one of the few regions of the world ocean where dense water formation (DWF) and deep convection down to the seafloor (2500 m depth) may occur during winter [*Schott et al.*, 1996]. Consequently this region is a key location for the thermohaline circulation of the whole basin. During winter the gale force northerly (Mistral) and north-westerly (Tramontane) winds induce strong surface buoyancy losses [*Lebeaupin-Brossier and Drobinski*, 2009; *Small et al.*, 2012] which trigger the convection and the formation of the Western Mediterranean Deep Water (WMDW: 12.9°C; 38.485; $\sigma > 29.0$ kg m^{-3}) [*Lascaratos et al.*, 1999] in the Gulf of Lion (GL). In response to the extreme cooling and evaporation at the surface in the GL, the cyclonic gyre—formed by the Liguro-Provençal Current in the North and the Balearic Front in the South—is reinforced by geostrophic adjustment around the convection area [*Millot*, 1999, *Hamad et al.*, 2005].

The scheme where the surface buoyancy flux destroys the stratification and trigger DWF and convection at the center of the cyclonic gyre in the GL is well-known and was described by *Madec et al.* [1991] and *Marshall and Shott* [1999]. Nevertheless the processes of destratification/restratification along the rim of the cyclonic gyre, precisely where the lateral density gradients and currents are strong, remain poorly understood.

Many density fronts in the world ocean, such as the Gulf Stream and Kuroshio systems, undergo strong surface winds and intense buoyancy and momentum fluxes. Interactions of atmospheric forcing with outcropping of the pycnocline at these fronts induce the formation and subduction of mode waters which may play an important role in the variability of the climate system [*Latif and Barnett*, 1994].

Mode waters are characterized by low stratification and low Potential Vorticity (PV). As pointed out by *Thomas and Ferrari* [2008], the PV is a crucial quantity to study the ocean dynamics because it establishes an univocal mass-circulation relationship through the invertibility principle [*Hoskins et al.*, 1985].

Consequently, PV strongly constrains the circulation. In frontal region with no atmospheric forcings, PV is conserved and the deformation frontogenetic field modifies the stratification through a spatial redistribution of PV. When diabatic and frictional atmospheric fluxes force a frontal region, the change in stratification results from the destruction or creation of PV at the surface, which is then redistributed into the ocean by the circulation. For instance, *Thomas* [2008] showed that the formation of intrathermocline eddies in an academic frontal jet is explained by frictional PV destruction at the surface. Likewise, the Eighteen Degree modal Water (EDW) located in the recirculation gyre south of the Gulf Stream [*Forget et al.*, 2011] is produced along the Gulf-Stream path rather by frictional PV destruction than by diabatic PV destruction at the surface [*Maze and Marshall*, 2011]. Based on PV-flux arguments, *Thomas and Marshall* [2005] suggested that the EDW is created in the [17°C−19°C] outcrop window, where the lateral buoyancy gradient and hence the frictional PV destruction is strong. Once created, this baroclinically low-PV water is transported downstream and expelled off the front, where PV is converted into a low-stratification which characterizes the EDW. Therefore, the EDW results from a nonlocal process along the Gulf-Stream that destroys the PV. *Thomas and Marshall* [2005] also suggested that a PV budget encompassing the EDW may be a more accurate metric than the *Walin* [1982]'s framework for estimating dense water formation in frontal region.

In the Kuroshio Current, *Rainville et al.* [2007] showed that the diabatic PV-destruction dominates the frictional PV-destruction in the formation of the Subtropical Mode Water (STMW) at regional scale, while the opposite occurs at mesoscale during strong downfront cold winds. The growing role of friction on the buoyancy in PV-destruction of frontal systems, eddies, and filaments is consistent with studies showing that the ocean dynamics at equatorial and midlatitudes is strongly controlled by the wind-work at the surface [*Klein et al.*, 2004; *Giordani et al.*, 2013]. These results confirm the need to study coupled air-sea processes at finescale (C. Lebeaupin-Brossier et al., Dense water formation in the North-Western Mediterranean area during HyMeX-SOP2 in 1/36° ocean simulations: Ocean-atmosphere coupling impact, in revision).

Less attention has been paid to PV budget to identify the processes which produce dense water in the mesoscale and submesoscale features in interaction with the wind in the Western Mediterranean. This paper proposes to extend the academic work of *Thomas and Lee* [2005], *Thomas* [2008] to the real case documented during the HyMeX/SOP2 experiment [*Estournel et al.*, 2016] in order to identify the submesoscale processes (particularly the diabatic and frictional PV-fluxes) of dense water formation in the frontal zone linked to the cyclonic gyre in the GL.

The HyMeX project (Hydrological cycle in the Mediterranean Experiment) [*Drobinski et al.*, 2014] investigated the hydrological cycle in the North-Western Mediterranean region during the autumn 2012 and winter 2013. The second Special Observing Period (SOP2: 1 February to 15 March 2013) in the GL [*Estournel et al.*, 2016] was dedicated to the documentation of DWF. Several atmospheric and ocean platforms were deployed during SOP2. This campaign is a challenging opportunity to investigate the submesoscale processes involved in DWF which occurred during winter 2013 in the GL.

This paper aims at identifying the processes of dense water formation along the baroclinic rim of the cyclonic gyre during the HyMeX/SOP2 experiment. To achieve this goal, a PV-budget of dense water formation is performed from a high-resolution regional ocean model implemented in the North-Western Mediterranean.

2. Numerical Design

2.1. The NEMO-WMED36 Model

The numerical hydrostatic ocean model NEMO [*Madec*, 2008] is used in a regional eddy-resolving configuration and is implemented over the western mediterranean basin with a 1/36° horizontal resolution (∼2−2.5 km) [*Lebeaupin-Brossier et al.*, 2014; *Léger et al.*, 2016]. First baroclinic Rossby radii of deformation (R_d) were computed using the so-called WKB method [*Chelton et al*, 1998] and 10 Argos floats profiles present in the western Mediterranean during February 2013. R_d ranges from 1.2 to 3.2 km that stresses the challenge for modeling the submesoscale. This version, so-called hereafter WMED36, has 50 stretched z-levels on the vertical with level thickness ranging from 1 m at the surface and 400 m at the sea bottom around 4000 m depth. The model has two radiative open boundaries, on the west at ∼4.8°W (60 km east of the Strait of Gibraltar) and on the south across the Sicily Channel (∼37°N). The Strait of Messina between Sicily and Italy is closed. The radiation condition at the open boundaries is applied to the prognostic variables of the

model. A phase speed is computed from *Orlanski* [1976] which propagates the information through the lateral boundaries of the domain with minimal reflection and spurious numerical waves.

The horizontal eddy viscosity coefficients are fixed at -1×10^9 m^2 s^{-1} for the dynamics and 30 m^2 s^{-1} for the tracers and the use of a bi-Laplacian and Laplacian operators, respectively. The TVD (Total Variance Dissipation) scheme is used for tracer advection in order to conserve energy and enstrophy [*Barnier et al.*, 2006]. The turbulent vertical mixing scheme is based on a parameterization of a second-order turbulent moments expressed as a function of the turbulent kinetic energy [*Gaspar et al.*, 1990] which was implemented into the NEMO code by *Blanke and Delecluse* [1993]. The convection is roughly represented by an increase of the coefficient of vertical diffusion [*Lazar et al.*, 1999] by 10 m^2 s^{-1} in case of static instabilities. The sea surface height is a prognostic variable which is solved by using the filtered free-surface scheme of *Roulet and Madec* [2000]. A no-slip condition is applied at the bottom and the bottom friction is parameterized by a quadratic function with a coefficient depending on the 2-D mean tidal energy [*Lyard et al.*, 2006; *Beuvier et al.*, 2012].

The initial and boundary conditions were provided by the PSY2V4R4 analysis performed by the operational system of Mercator-Océan PSY2. This analysis covers the North-East Atlantic Ocean, the North and Baltic Seas, and the Mediterranean Sea at the resolution 1/12°.

Data collected by the Lion and Azur buoys; Argo floats; ships of opportunity (XBT); gliders; satellite SST (AVHRR) [*Reynolds et al.*, 2007]; and altimetry sensors are currently assimilated by the operational system. In situ observations available in real time at the Coriolis Center (http://www.coriolis.eu.org/) are subsampled: for each platform, a single profile is retained within a spatial radius of 0.1° and a temporal radius of 24 h. The data assimilation method relies on a reduced-order Kalman filter based on the singular evolutive extended Kalman filter (SEEK) formulation [*Lellouche et al.* 2013].

The surface Atlantic water and the Levantine intermediate water inputs across the strait of Gibraltar and the Sicily channel, respectively, are controlled through the PSY2V4R4 boundary conditions. The river and costal runoffs are prescribed from a climatology [*Beuvier et al.*, 2010] and applied at the surface. For more details, see *Léger et al.*, [2016] and Lebeaupin-Brossier et al. (in revision).

The model WMED36 is forced at the surface by the hourly AROME-WMED forecasts from the 1 September 2012 to the 15 March 2013. The nonhydrostatic and convection-permitting AROME-WMED model [*Fourrié et al.*, 2015] with a 2.5 km-resolution grid was dedicated to the HyMeX field campaigns, doing in real-time daily forecasts covering both the first HyMeX Special Observations Period (SOP1, from 5 September to 6 November 2012) [*Ducrocq et al.*, 2014] to the end of SOP2 (from 1 February to 15 March 2013).

Additional information on the models NEMO-WMED36 and AROME-WMED and extended validations of these models against in situ data collected during the SOP2 of the HyMeX experiment can be found in *Lebeaupin-Brossier et al.* [2014] and *Léger et al.* [2016]. In particular, *Léger et al.* [2016] showed that the simulated mixed-layer depths (MLD), defined as the depth with a density gap with the surface of 0.01 kg m^{-3}, are quite realistic compared with in situ profiles (Argo floats and CTD profiles of R/V *Le Suroît*) [see *Léger et al.*, 2016, Figures 5 and 6] and volumes of dense water produced ($\sigma > 29.0$ kg m^{-3}) during winter 2013 are realistic compared with estimations deduced from in situ data [*Waldman et al.*, 2016].

2.2. Dense Water Formation

The positioning of winter 2013 in a broader temporal climatological context of the last 15 years is estimated from the monthly surface net heat flux (F_{net}) of ERA-Interim reanalysis interpolated at the Lion buoy (Figure 1). The Lion meteorological buoy is a reference for validation because it is a long-term observatory system in the GL to monitor the convection in the mixed-patch since 2002 [*Houpert et al.*, 2016]. The ERA-I reanalysis is in agreement with in situ data at the Lion buoy when considering only the sum of latent and sensible fluxes because of not long enough measured radiative data to compute a net heat flux climatology for a long period. In spite of this lack, measurement and reanalysis are very close for surface heat fluxes (-257 W m^{-2}/-244 W m^{-2}) and wind-stress (0.334 N m^{-2}/0.323 N m^{-2}) (not shown).

The climatology (2000–2015) of F_{net} shows that the strongest energy losses occur in December (-201 W m^{-2}), November (-170 W m^{-2}), and January (-162 W m^{-2}), respectively. Regarding the surface wind-stress, the temporal distribution of strongest intensities is a little bit different than for F_{net} since it occurs in December (0.21 N m^{-2}), February (0.197 N m^{-2}), and January (0.19 N m^{-2}) (not shown).
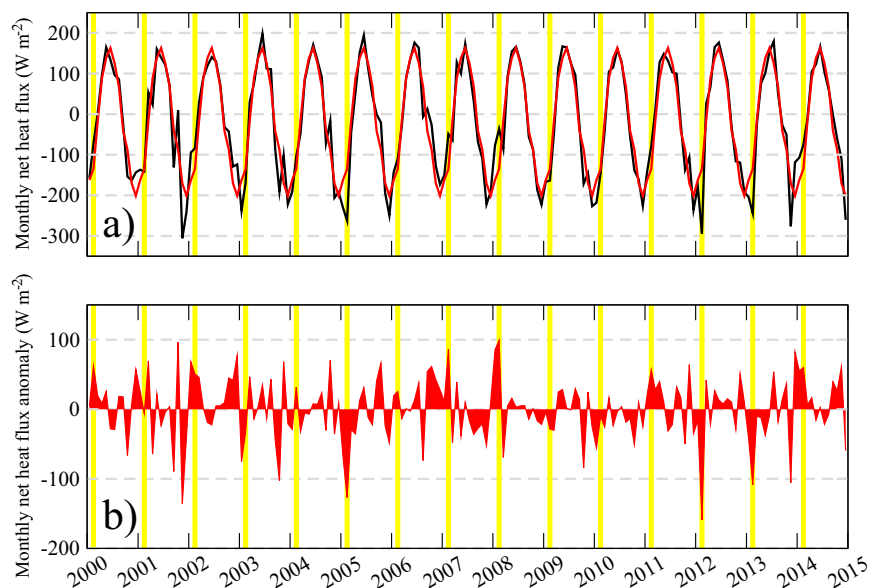
Figure 1. (a) Monthly surface net heat flux (W m^{-2}) of ERA-Interim reanalysis (black line) and monthly ERA-I climatology (red line) at the Lion buoy. (b) Anomalies are in red. Yellow bands mark the months of February 2013.

In February 2013, F_{net} went down to -244 W m^{-2}, namely an anomaly of -109 W m^{-2} compared to the 2000–2015 climatology. Likewise, the surface wind-stress reached its maximum of 0.323 N m^{-2} which represents an anomaly of 0.126 N m^{-2} compared to the climatology in February.

It is noteworthy to note from Figure 1 that years with the strongest anomalies in February correspond to the most intense convective years like in 2005, 2012, and 2013 [*Houpert et al.*, 2016], while the climatology indicates that the Northwestern Mediterranean starts its restratification during this period. Consequently, the severity in the atmospheric surface forcings in late winter (i.e., February) seems to be a good index to characterize convective years, whereas fall atmospheric conditions cannot help to anticipate convective or not convective year.

As shown by *Marshall and Shott* [1999], the sustained losses of buoyancy at the surface are key ingredients for dense water formation in the GL in winter, but the ERA-I climatology indicates that February is a crucial month for convective activity. This is the reason why this study is focused on February 2013 during which intense deep convection was observed [*Houpert et al.*, 2016].

Intense surface energy losses provided by the atmospheric model AROME occurred in the GL and reached at minimum -400 W m^{-2} on average during February 2013 (Figure 2) under the path of Mistral and Tramontane dominant winds. These buoyancy fluxes were associated with the dominant north and northwesterly winds Mistral and Tramontane as shown in Figure 2. The month-averaged surface wind-stress curl displayed in Figure 2 is a proxy of the Ekman pumping. An ascending positive (subsiding negative) pumping zone is present on the right cyclonic (left anticyclonic) side of dominant winds. The two areas of opposite sign are separated by a nearly 120 km wide corridor corresponding to the main pathway of the dominant winds in the area. The north-eastern area with positive pumping plays an important role for preconditioning water masses, by maintaining the doming of isopycnals inside the gyre interior, as underlined by *Gascard* [1978], *Madec et al.* [1996], and G. Caniaux et al. (An inverse method to derive surface fluxes from the closure of oceanic heat and water budgets: application to the North-western Mediterranean Sea, in revision) in the GL. As consequence favorable atmospheric conditions (intensity and timing) were present during the HyMeX/SOP2 for dense water formation. Now we look at the spatial distribution of dense water formed during February 2013.

Dense waters produced in class C_1—which correspond to density $\sigma \in [29.0 - 29.13]$ where $\sigma = 29.13$ kg m^{-3} is the maximum value of the density produced in February 2013—are representative of the WMDW and named DWF_1. DWF_x is the volume variation in class C_x between 28 February and 1 February. Positive
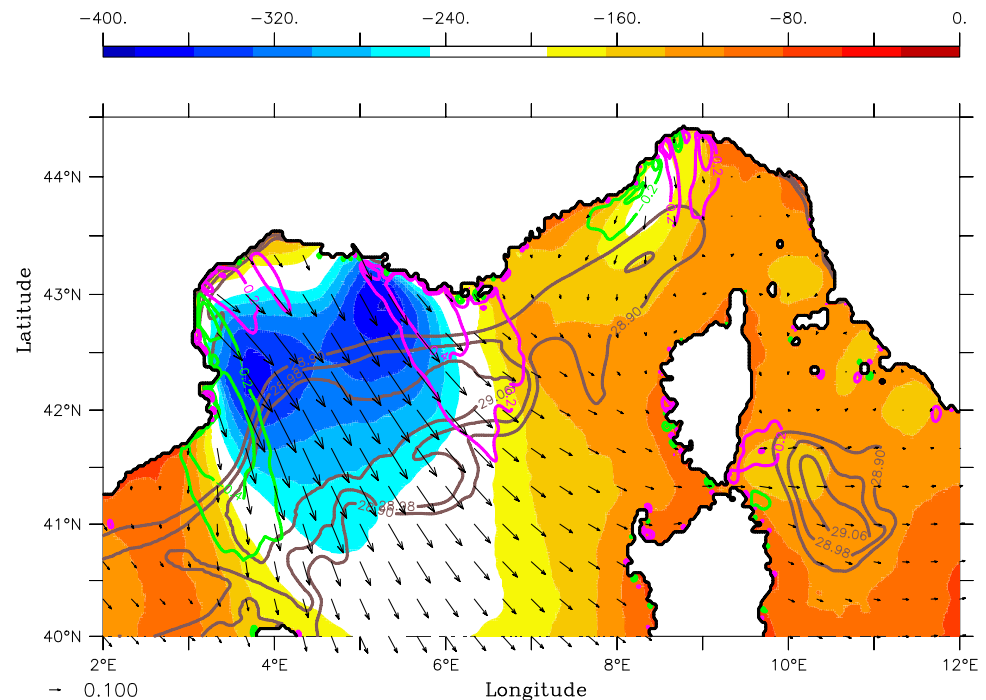
Figure 2. February 2013 averaged simulated surface buoyancy flux (colour, W m^{-2}) superimposed with the surface density (brown lines, σ > 28.9 kg m^{-3}; interval 0.08 kg m^{-3}); the surface wind-stress curl (cyan positive, green negative values, N m$^{-3} \times 10^5$; interval 0.2×10^{-5} N m$^{-3} \times 10^5$) and the surface wind-stress (black arrows, N m^{-2}).

(negative) values of DWF_x mean production (destruction) of water in class C_x. Surprisingly the spatial distribution of DWF_1 (Figure 3a) does not occur at the center of the cyclonic gyre but along the rim of the gyre i.e., in the baroclinic zone where the density gradients and currents are strong. In fact the production is expected at the center of the gyre where convection occurs and not around. In order to show the central production, DWF_1 is split into two components DWF_2 and DWF_3 ($DWF_1 = DWF_2 + DWF_3$) which correspond to waters produced in classes C_2 : $\sigma \in [29.0 - 29.12]$ and C_3 : $\sigma \in [29.12 - 29.13]$ kg m^{-3}, respectively (Figures 3b and 3c). Class C_2 and C_3 separate moderate dense water which occurs almost every year from extreme dense water which occurs some years, respectively [*L'Hévéder et al.*, 2013; *Léger et al.*, 2016]. DWF_2 and DWF_3 display areas of strong destruction and production, respectively, at the center of the gyre and the sum tends to cancel almost perfectly because of their similar intensities and patterns. This behavior highlights the water mass transformation from class C_2 to class C_3. As a consequence of this cancelation, the net production DWF_1 occurs along the rim of the gyre. The magnitude of the lateral production is 2×10^9 m^3 and represents around 10% of the central production of DWF_3 (20×10^9 m^3) shown in Figure 3c.

Evolutions of the spatial-integrated productions DWF_2 and DWF_3 during February show the abrupt destruction of class C_2 to the benefit of class C_3 on 24 February (Figure 4a). This is consistent with estimates of *Waldman et al.* [2016] and Lebeaupin-Brossier et al. (in revision). Water mass formation can be diagnosed from the surface heat flux following the method developed by *Walin* [1982] and extended by *Tziperman* [1986] who also considered freshwater fluxes. Thereby, the Tziperman's method allows to derive an upper bound for water mass formation from the surface buoyancy flux F_{buo}. The production rate for a water mass of potential density within a class C_x defined as $\sigma \in [\sigma_x, \sigma_x + \Delta\sigma]$ results from the surface buoyancy flux acting on the area $\Delta S = \Delta x \Delta y$ bounded by the outcropping density surfaces σ_x and $\sigma_x + \Delta\sigma$. This production rate writes as follows:

$$VSB_x = -\frac{\sigma}{g\Delta\sigma} \sum_{\sigma \in [\sigma_x, \sigma_x + \Delta\sigma]} F_{buo}(x,y)\Delta x \Delta y \Delta t$$

A positive value of VSB_x indicates water mass formation and negative value indicates water mass destruction.
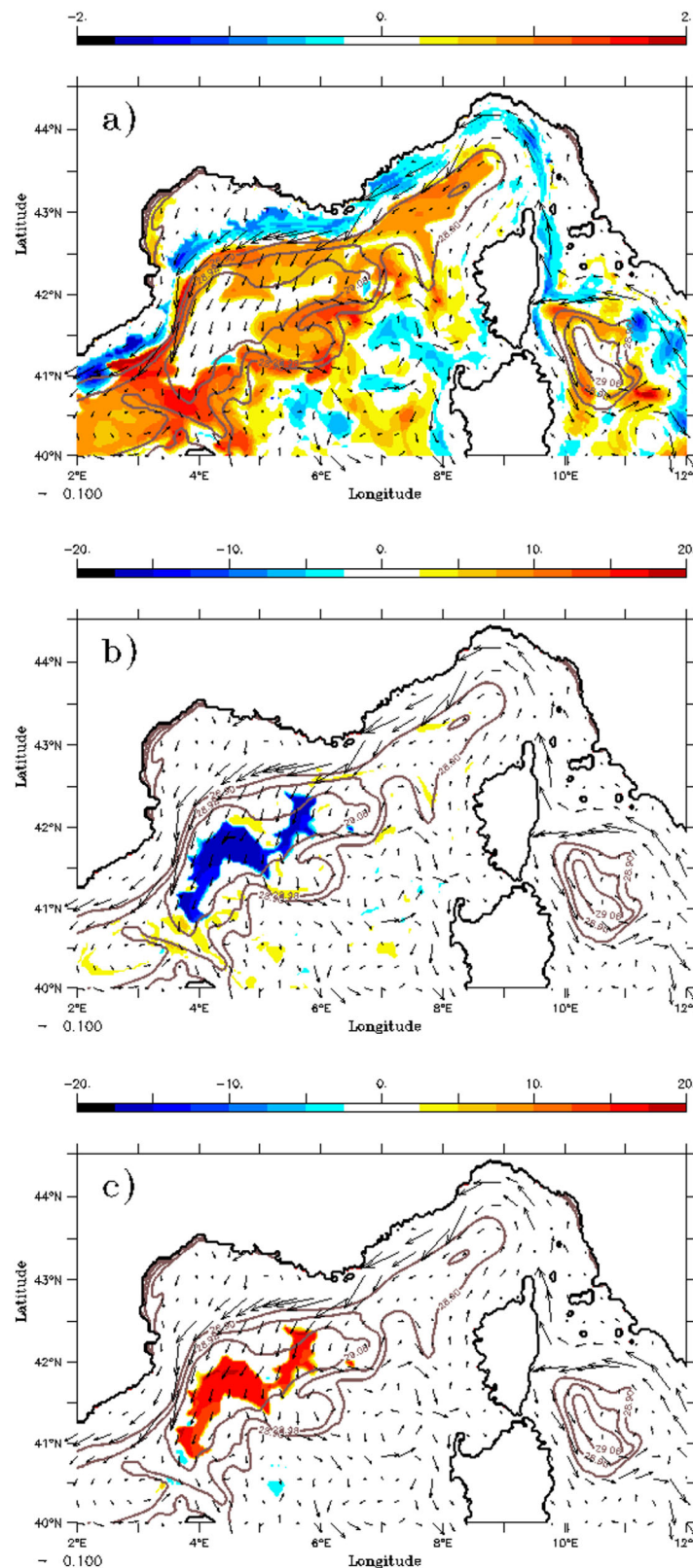
Figure 3. Dense water formation volume (m³×10⁻⁹) during February in the class: (a) C_1: $\sigma > 29$ kg m⁻³, (b) C_2: $\sigma \in [29.0 - 29.12]$, and (c) C_3: $\sigma > 29.12$, superimposed with the month-averaged surface density (contours, kg m⁻³) and surface current (arrows, m s⁻¹) fields.
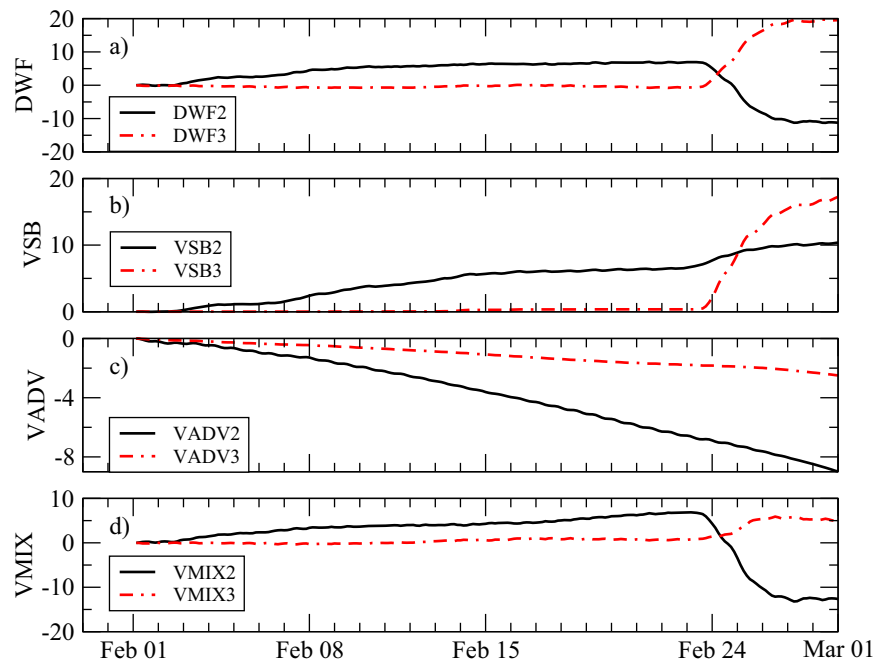
Until 24 February, the integrated buoyancy volume VSB_2 of class C_2 (Figure 4b) increases and pretty well captures the trend of DWF_2. From 24 February, DWF_2 drops while DWF_3 simultaneously increases sharply: this points out the water mass transformation from class C_2 to C_3. However, VSB_2 does not change trend, it becomes opposite to the trend of DWF_2 and VSB_3 suddenly appears with the emergence of class C_3. During February the monotonic increase of VSB_2 is due to continuous negative surface buoyancy flux (buoyancy loss) combined with surface density in class C_2. Class C_2 is sustained at the surface probably on account of light water advection by the southward current (Figure 3) from the continental shelf inward the gyre. This suggests that the production and destruction of dense water can be also the result from a dynamical process as shown by *Pasquet et al.* [2012].

Following *Walin* [1982], the water volume budget DWF_x of class C_x is controlled by the following conservation relationship

$$DWF_x = VSB_x + VADV_x + VMIX_x \quad (1)$$

$VADV_x$ is the advective diapycnal volume flux and $VMIX_x$ represents many mixing processes that result in diffusive flux across the isopycnal bounds σ_x and $\sigma_x + \Delta\sigma$ which define the control volume [*Speer et al.*, 2000]. In this study $VMIX_x$ is estimated as a residual term of the conversation relationship (1).

The negative trend of the integrated advective volume $VADV_2$ of class C_2 (Figure 4c) almost balances the positive trend of the buoyancy volume (VSB_2; Figure 4b). As consequence DWF_2 (Figure 4a) is mainly controlled by

Figure 4. Evolution during February of the water budget (m$^3 \times 10^{-12}$) in classes C_2 ($\sigma \in [29.0-29.12]$) and C_3 ($\sigma > 29.12$). (a) Dense water formation, (b) surface buoyancy flux, (c) advection, and (d) mixing.

the integrated mixing term ($VMIX_2$; Figure 4d). Until 24 February, the dense waters formed by surface buoyancy flux ($VSB_2 > 0$) and mixing ($VMIX_2 > 0$) are exported by advection ($VADV_2 < 0$). From 24 February, the dense waters formed by VSB_2 only are exported ($VADV_2 < 0$) and consumed by intense mixing ($VMIX_2 < 0$).

Regarding class C_3, the integrated advective volume $VADV_3$ (Figure 4c) reveals a permanent export of water by advection during February. This confirms the presence of class C_3 before its renewal on 24 February.
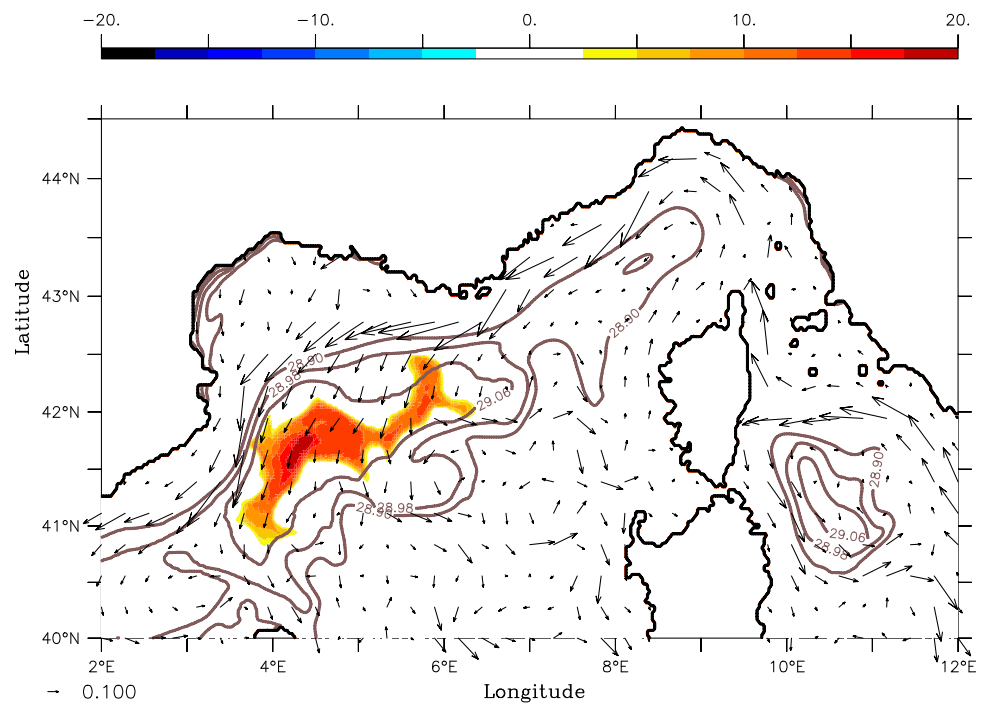
Figure 5. Dense water formation volume (m$^3 \times 10^{-9}$) deduced from the *Speer and Tziperman* [1992] method during February in the class C_3 ($\sigma > 29.12$ kg m^{-3}), superimposed with the month-averaged surface density (contours, kg m^{-3}) and current (arrows, m s^{-1}) fields.
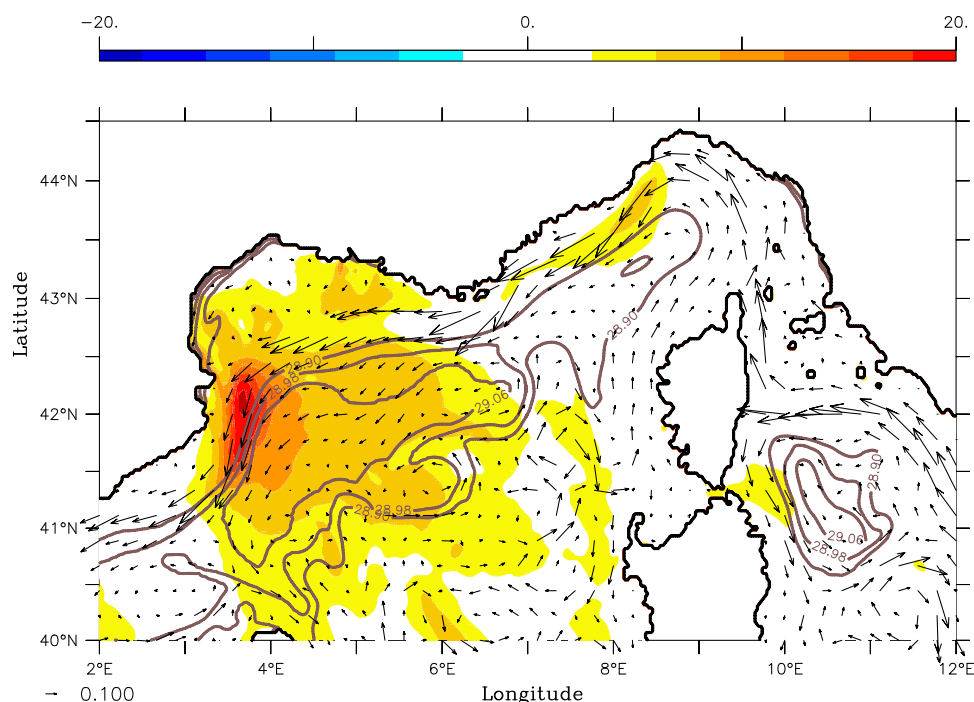
Figure 6. Month-averaged Wind Energy Flux (WEF, m^3 s^{-3}×10^5) superimposed with the month-averaged surface density (contours, kg m^{-3}) and current (arrows, m s^{-1}) fields. Maximum WEF is located along the Catalan coast i.e., along the northern branch of the North Current.

From 24 February, this export only slightly increases but is crushed by intense surface buoyancy flux ($VSB_3 > 0$; Figure 4b) and to a lesser extent by mixing ($VMIX_3 > 0$; Figure 4d).

Finally the advection and mixing terms are significant particularly in class C_2 during February which corresponds to the intense convection period. Such strengthening of advection during strong convection events was also found by *Herrmann et al.* [2008a,2008b].

In terms of spatial distribution, it is noteworthy that VSB_3 (Figure 5) is highly correlated with the fields DWF_2 and DWF_3 (Figures 3b and 3c) but with the opposite signs, respectively. This confirms the leading role of surface fluxes in the water transformation from class C_2 to C_3. These results are in agreement with numerous works, which have shown the central role of surface buoyancy fluxes in the dense water formation in shelf seas [*Badin et al.*, 2010] and the triggering of convection at the center of the gyre in the GL [*Marshall and Shott*, 1999; *Herrmann et al.*, 2008a; *Léger et al.*, 2016].

As the productions of DWF_2 and DWF_3 tend to cancel each other, the net dense waters are produced in the frontal zone of the North Current. This result pushes to look for underlying mechanisms. Some studies have shown that the ocean dynamics is significantly controlled by the kinetic energy flux injected into the ocean by the wind-stress [*Klein et al.*, 2004; *Giordani et al.*, 2013] (Lebeaupin-Brossier et al., in revision). This flux, also named Wind Energy Flux ($WEF = \vec{\tau} \cdot \vec{u}$), is positive (negative) when the atmosphere increases (decreases) the ocean mean kinetic energy $\left(\frac{u^2+v^2}{2}\right)$. The month-averaged WEF presented in Figure 6 is positive over the whole basin, meaning that the surface wind-stress is source of kinetic energy for the ocean. WEF-maxima are found in the baroclinic zone of the cyclonic gyre, in the Ligurian Sea and along the Catalan coast i.e., along the northern branch of the North Current, where dense waters are produced (Figure 3a). Patterns of WEF suggest that mechanical forcings are probably also candidates to produce dense waters as do surface buoyancy fluxes in the patch. This motivated to further investigate the mechanisms which produce dense water in the baroclinic rim of the cyclonic gyre.

3. Potential Vorticity Dynamics

PV is changed through the interactions of diabatic and momentum atmospheric forcing with velocity shears and buoyancy gradients at the ocean surface. Consequently, PV is an interesting variable for studying the

stratification/destratification mechanisms and dense water dynamics, where surface oceanic fronts permanently interact with the wind.

The variable considered is the full Ertel PV (q, s^{-3}) defined here as:

$$q = \vec{\omega}.\vec{\nabla} b \tag{2}$$

where $\vec{\omega} = f\vec{k} + \vec{\nabla} \wedge \vec{u}$ is the absolute vorticity, f the Coriolis parameter, $\vec{u}$ the vector current, and $b = -g\sigma/\sigma_0$ the buoyancy. Expanding equation (2) into its vertical and horizontal components leads to

$$q = \underbrace{(\zeta+f)N^2}_{q_v} + \underbrace{\vec{\omega_h}.\vec{\nabla}_h b}_{q_h} \tag{3}$$

where q_v and q_h represent the vertical and horizontal/baroclinic component of PV, respectively, and N the Brunt Vaisala frequency. Using the thermal wind balance, $f\frac{\partial u_g}{\partial z} \wedge \vec{k} = \vec{\nabla}_h b$, the horizontal/baroclinic component q_h of q writes as:

$$q_h = -f\left[\left(\frac{\partial u_g}{\partial z}\right)\left(\frac{\partial u}{\partial z}\right) + \left(\frac{\partial v_g}{\partial z}\right)\left(\frac{\partial v}{\partial z}\right)\right] \tag{4}$$

the geostrophic component of which is:

$$q_{hg} = -f\left[\left(\frac{\partial u_g}{\partial z}\right)^2 + \left(\frac{\partial v_g}{\partial z}\right)^2\right] \tag{5}$$

In this expression of the geostrophic baroclinic component, q_{hg} is always negative meaning that low-PV and even negative PV water can occur at fronts because the baroclinic component q_h can overcome the vertical component q_v.

The flux-form of the PV equation is:

$$\frac{\partial q}{\partial t} = -\vec{\nabla}.\vec{\mathcal{J}} \tag{6}$$

The total PV flux $\vec{\mathcal{J}}$ (ms^{-4}) is defined by:

$$\vec{\mathcal{J}} = \vec{u}q + \vec{\nabla}b \wedge \frac{\partial \vec{\tau}}{\partial z} + \vec{\omega}\frac{\partial \vec{B}}{\partial z} \tag{7}$$

where $\vec{\tau}$ and $\vec{B}$ are the vertical momentum and buoyancy fluxes, respectively. $\vec{\mathcal{J}}$ has three components which are:

$$\begin{cases} \vec{\mathcal{J}}_{adv} = \vec{u}q & \text{Advective PV flux} \\[2mm] \vec{\mathcal{J}}_{fric} = f\frac{\partial \vec{u_g}}{\partial z}\frac{\partial \vec{\tau}}{\partial z} & \text{Frictional PV flux} \\[2mm] \vec{\mathcal{J}}_{diab} = (\zeta+f)\frac{\partial \vec{B}}{\partial z} & \text{Diabatic PV flux} \end{cases} \tag{8}$$

PV-destruction at the air-sea interface occurs when the surface PV-fluxes $\vec{\mathcal{J}}_{diab}$ and $\vec{\mathcal{J}}_{fric}$ are positive. $\vec{\mathcal{J}}_{diab}$ is positive for a surface buoyancy loss ($B > 0$) which induces a destruction of stratification [*Marshall and Schott*, 1999]. $\vec{\mathcal{J}}_{fric}$ is positive when the surface wind-stress and geostrophic current shears are oriented in the same direction. Therefore in presence of a density front, PV destruction occurs when the wind blows downfront *Thomas and Lee* [2005]. In such condition, the destratification at front sets up by advection of dense water over light water by the Ekman current [*Thomas and Ferrari*, 2008].

4. PV Budget

The month-average surface buoyancy flux (Figure 2) displays intense energetic losses down to -400 W m^{-2} in the GL and down to -200 W m^{-2} in the Ligurian Sea along the North Current. On 24 February, the near-surface PV field (Figure 7) displays negative structures located in frontal areas i.e., in the North Current and the eddying Balearic front: these structures are induced by the horizontal/baroclinic component q_h of PV.
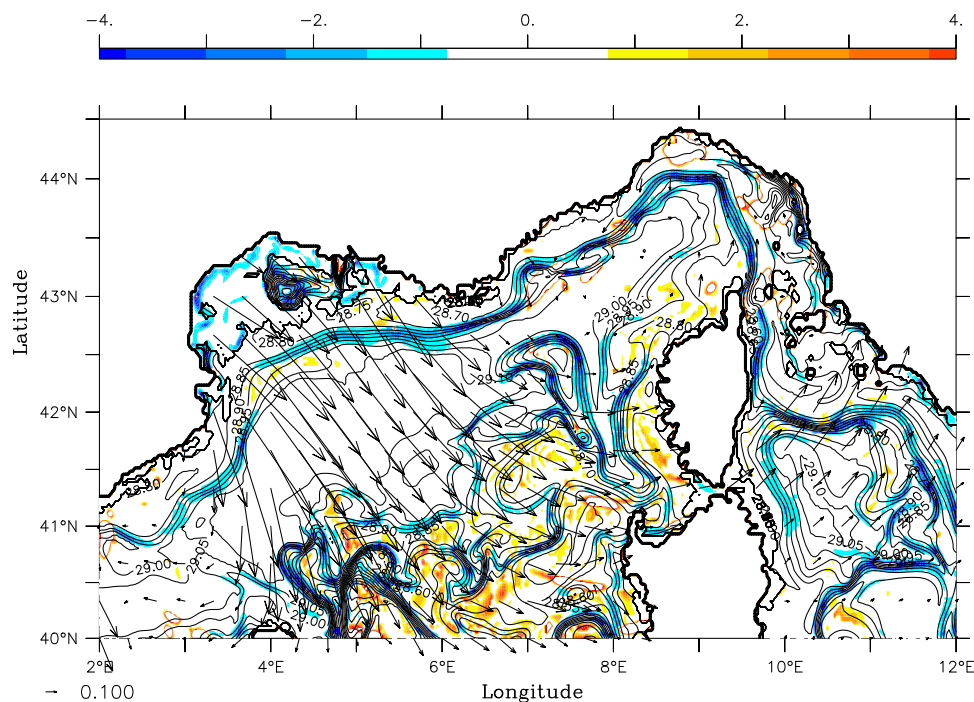
Figure 7. Daily averaged near-surface PV ($s^{-3} \times 10^{10}$) superimposed with surface density (contours, $kg\,m^{-3}$) and surface wind-stress (arrows, $N\,m^{-2}$) fields on 24 February.

The question which arises is: what is the role of the surface wind-stress and buoyancy flux in the generation of such negative structures? This question is now treated by studying the PV budget.

During February, the decrease of the volume integrated PV bounded by the isopycnal $\sigma = 29.0\ kg\,m^{-3}$ is closely anticorrelated with the volume of dense water formation (Figures 8a and 8b). Three periods of marked PV-destruction can be identified on 2–4, 6–14, and 23–26 February, which correspond to strong wind and flux events that produced dense water. These results confirm the tight link between PV-destruction and dense water formation (Figure 8c).

In terms of spatial distribution, PV-destruction (Figure 9) occurs in baroclinic zones where the dense waters are produced (Figure 3a) in February. This spatial representation confirms the tight connection between PV-destruction and dense water formation already highlighted in the temporal representation. The similar patterns of PV and N^2 variations (not shown) indicate that PV-destruction is associated with destratification. This result is consistent with the alternative equation for the rate of change of stratification based on PV fluxes derived by *Thomas and Ferrari* [2008].

Understanding the sources and sinks of PV requires to consider the PV-equation (6) integrated over the volume ($\mathcal{V}$) bounded by the isopycnal $\sigma > 29.0\ kg\,m^{-3}$. The budget is performed following the equation used by *Thomas* [2008]:

$$\Delta \int_{\mathcal{V}} dq dV = \underbrace{-\int_{\mathcal{V}} \vec{u} . \vec{\nabla} q dV dt}_{J_{adv}} + \underbrace{\int_{\mathcal{V}} f \left(\vec{\nabla} \wedge \frac{\partial \vec{\tau}}{\partial z} \right) \left(\frac{\partial \vec{u_g}}{\partial z} \wedge \vec{k} \right) dV dt}_{J_{fric}} - \underbrace{\int_{\mathcal{V}} (\zeta + f) \frac{\partial^2 B}{\partial z^2} dV dt}_{J_{diab}} \qquad (9)$$

where Δ denotes the volume integrated PV variation between the current and initial times. The PV-budget components on the right hand side of equation (9) are now inspected.

The spatial distribution of the nonadvective PV-flux ($J_{flux} = J_{fric} + J_{diab}$), including the frictional and diabatic/buoyancy terms is negative around the gyre precisely where dense waters are produced (Figure 10a). The diabatic/buoyancy PV-flux (J_{diab}) (Figure 10c) dominates on average the destratification and dense water production around the gyre because of strong buoyancy losses associated with cold and dry air advection (Figure 2). Note that J_{fric} (Figure 10b) is often positive around the convective patch meaning a restratification of the
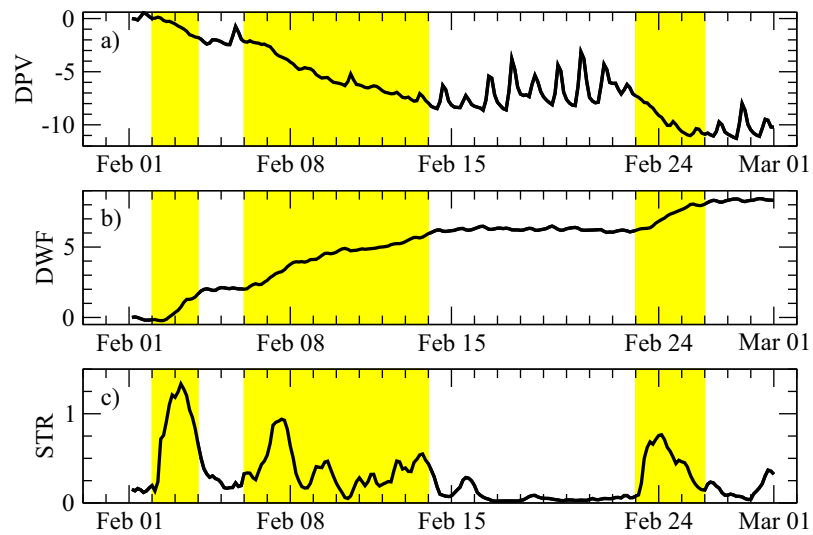
**Figure 8.** February time series of (a) the volume integrated PV (DPV, m^3 s^{-3}×10^{-3}); (b) the volume of dense water formation (DWF, m^3×10^{-12}) bounded by the isopycnal $\sigma \geq 29$ kg m^{-3}; and (c) the surface wind-stress (STR, N m^{-2}). Yellow bands mark the periods of strong Mistral and Tramontane northerly winds.

ocean by wind. This corresponds to PV-input into the ocean because of opposite current shear and wind directions. If the full diabatic PV-flux is negative (Figure 10c), the contribution of the turbulent PV-entrainment at the pycnocline ($J_{diabent}$) to J_{diab} is contrariwise positive in the frontal region (Figure 10d). Likewise, the horizontal PV-advection (J_{advh}, Figure 10e) and the turbulent PV-entrainment (Figure 10d) are both positive and opposite to the nonadvective PV-flux J_{flux} (Figure 10a) at the rim of the gyre.

Generally J_{diab} prevails on J_{fric}, except along the northern branch of the North Current. Around [4°E−42°N] the dense water formation is controlled by the frictional PV-flux (J_{fric}) because the destratification is mainly driven by mechanical interactions between the northern Mistral and Tramontane winds and the lateral
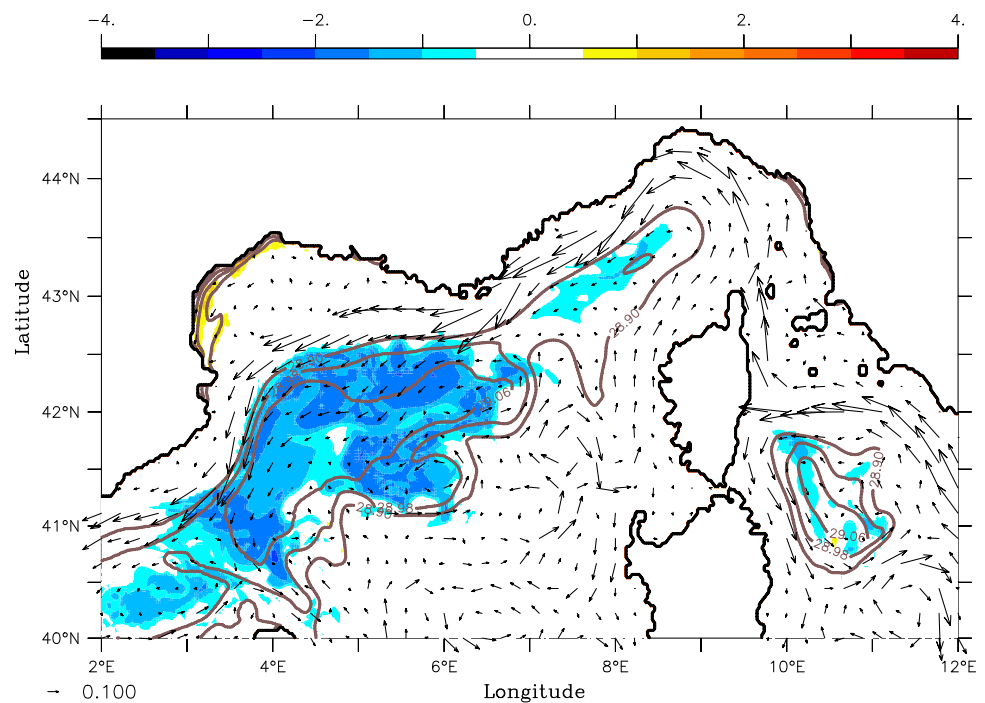

Figure 9. Integrated February PV-budget (m^3 s^{-3}) superimposed with the surface density (contours, kg m^{-3}) and current (arrows, m s^{-1}) fields.
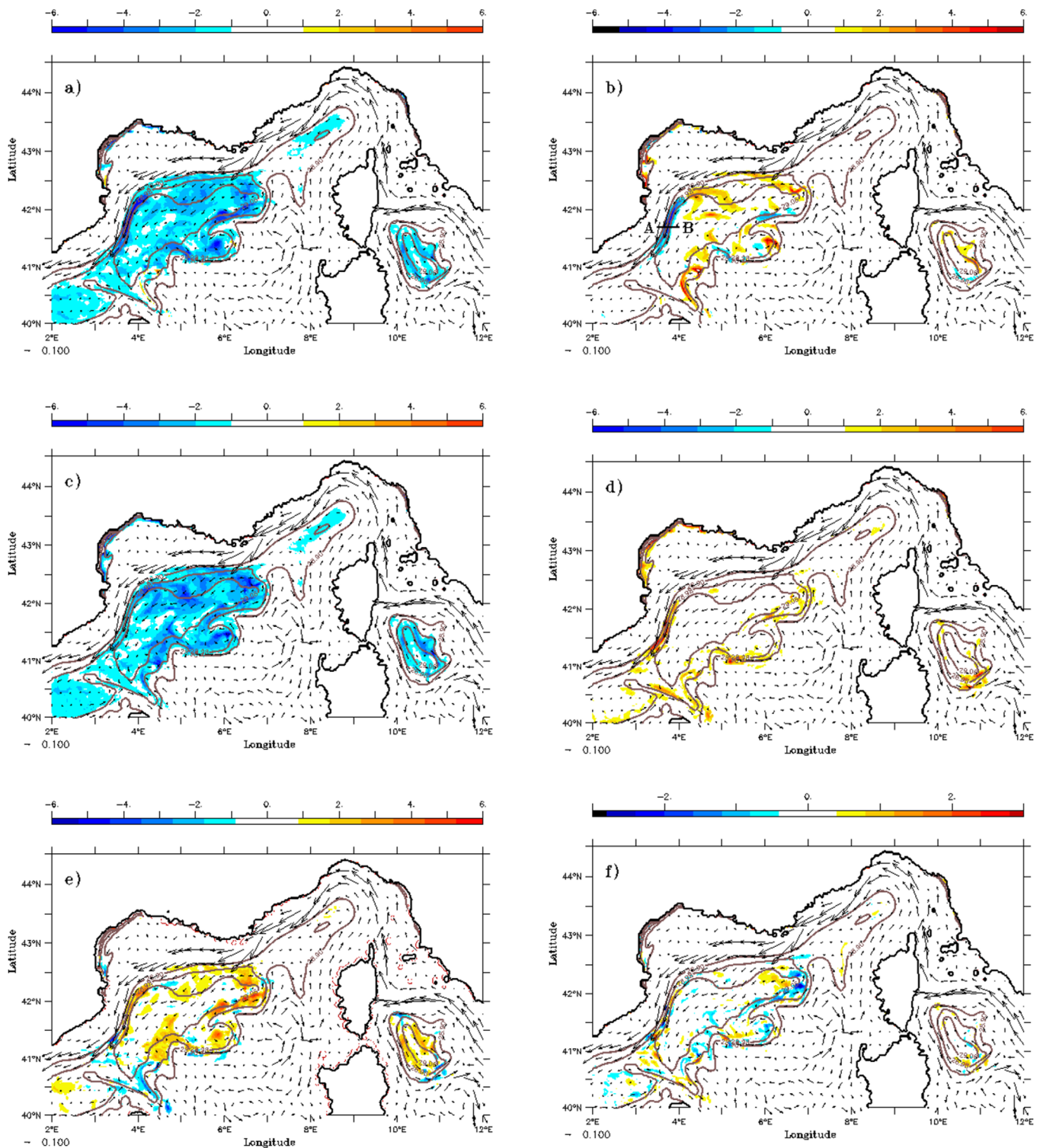
Figure 10. Components of the PV-budget (m^3 s^{-3}) (a) J_{flux}, (b) J_{fric}, (c) J_{diab}, (d) $J_{diabent}$, (e) J_{advh}, and (f) J_{advv} superimposed with the surface density (contours, kg m^{-3}) and current (arrows, m s^{-1}) fields. Segment [A-B] on Figure 10b represents the cross-front vertical section presented in Figure 11.

density gradient associated with the front (Figure 10b). J_{fric} is source of PV-destruction because the surface current and predominant winds are in the same northern directions.

Along the northern branch of the North Current, the vertical PV-advection (J_{advv}, Figure 10f), which is twice lower intensity, is alternatively positive and negative because the front is destabilized by the prevailing
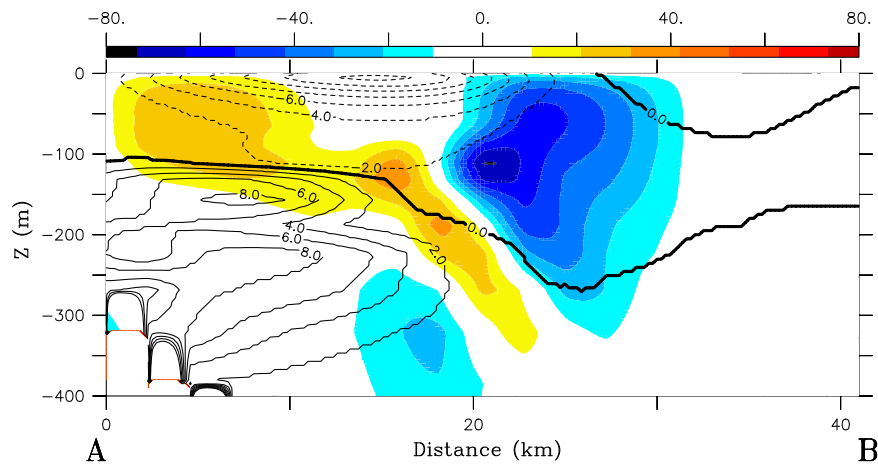
Figure 11. Vertical section of the vertical velocity (color, $m\,d^{-1}$) superimposed with the potential vorticity (contours, $s^{-3} \times 10^{10}$) on 7 February. The position of section [A-B] is indicated in Figure 10b.

northerly wind in February. In this area, the surface PV-destruction induced by the forcing J_{flux} (Figure 10a) makes the front unstable and gives rise to an ageostrophic circulation across the front, which tends to restore the thermal wind-balance destroyed by the wind [*Giordani et al.*, 2006; *Thomas*, 2007]. This adjustment is illustrated in the vertical section through the northern branch of the North Current which extends in the longitude band $[3.5°E{-}4°E]$ at the latitude $41.7°N$ on 7 February (Figure 11), one of the three windy periods. That day, the strong northerly winds (Tramontane regime) give favorable conditions for PV-destruction because the wind and current are more or less constantly in the same directions. In this section the dipole of vertical velocity (w) signs the presence of an ageostrophic cell across the front which is downward on the dense side (surface low-PV water) and upward on the light side (subsurface high-PV water) of the front (Figure 11). Maxima downwelling ($\sim{-}80\,m\,d^{-1}$) and upwelling ($\sim40\,m\,d^{-1}$) are located in the first 100 m depth; this is consistent with subsurface vertical motions in fronts constraint by intense lateral strain
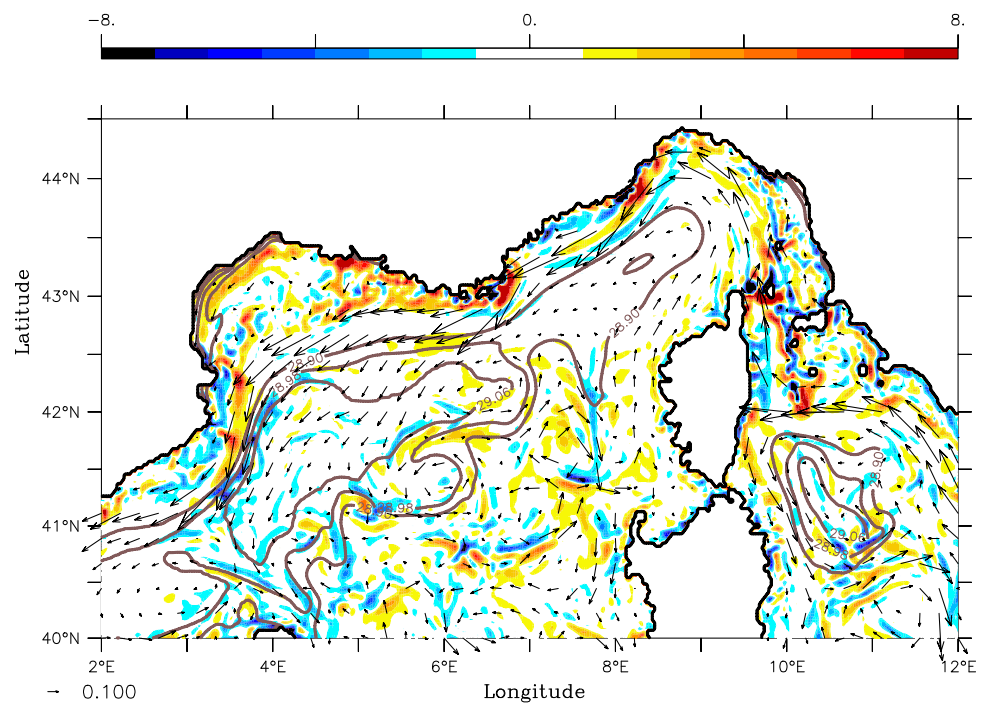
Figure 12. Mean vertical velocity ($m\,d^{-1}$) at 30 m depth during the month of February superimposed with the surface density (contours, $kg\,m^{-3}$) and current (arrows, $m\,s^{-1}$) fields.
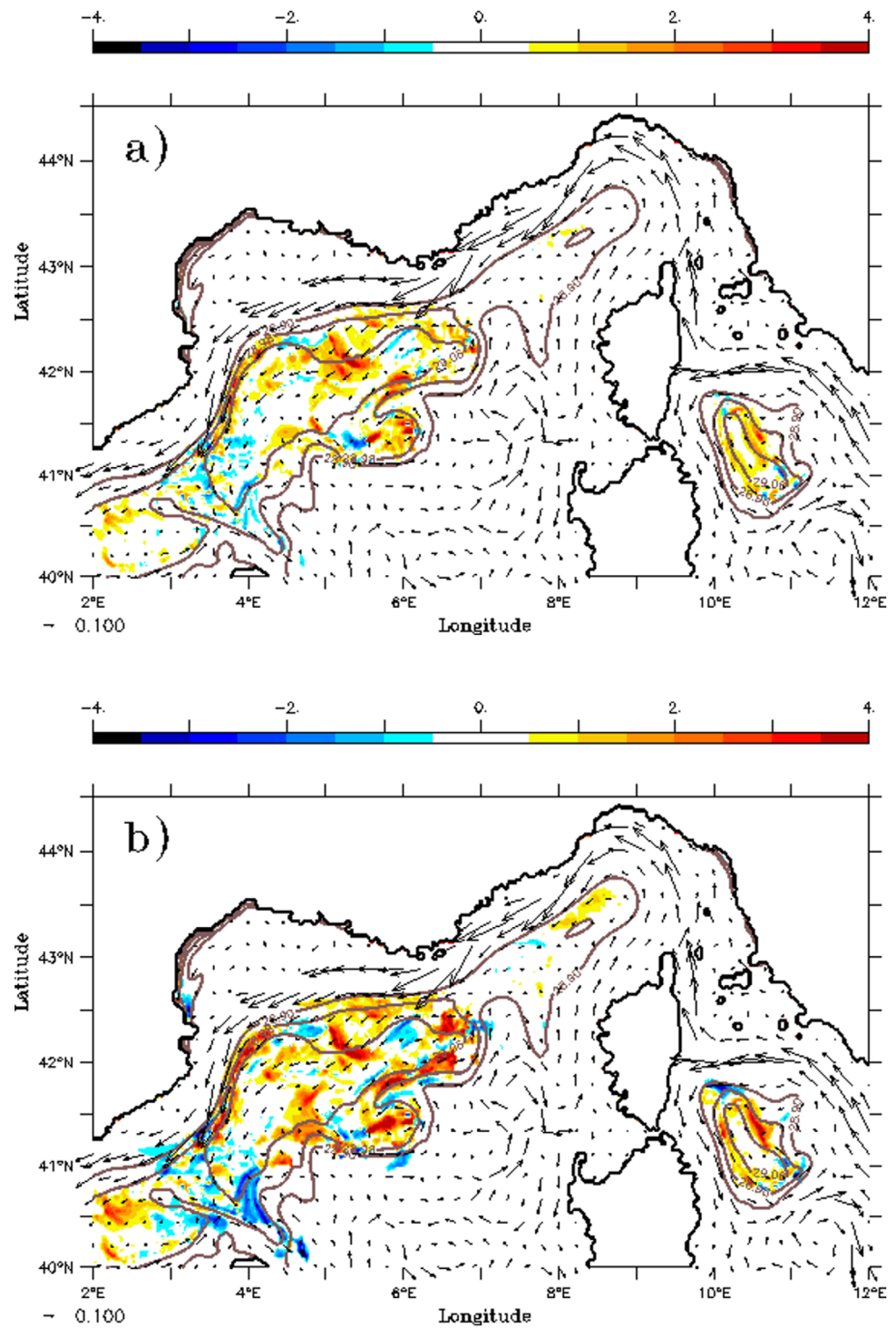
Figure 13. PV-advection (m³ s⁻³) (a) low-frequency $J_{advh_{lf}}$, (b) high-frequency $J_{advh_{hf}}$ superimposed with the surface density (contours, kg m⁻³) and current (arrows, m s⁻¹) fields.

[*Mahadevan and Tandon*, 2006]. This cell is robust because it is present at monthly scale, not only along the northern branch of the North Current but also all around the gyre (Figure 12).

As mentioned previously, the strongest PV-advections (J_{advh}) are found in frontal zones of the gyre (Figure 10e). However these structures are not confined in the baroclinic area but propagate inward the cyclonic gyre. This transport is probably associated by eddies generated by baroclinic instability of the front. In order to capture

the time-integrated effects of these eddies on the stratification of the gyre, the PV-advection J_{advh} is separated into a low and high-frequency components as in *Foltz et al.* [2003], *Peter et al.* [2006], and *Giordani et al.*, [2013]:

$$
\begin{cases}
J_{advh} = -\underbrace{\int_{\mathcal{V}} \overline{\mathbf{U}}_h . \nabla \bar{q} \, dV dt}_{J_{advh_{lf}}} - \underbrace{\int_{\mathcal{V}} \overline{\mathbf{U}\prime_h \nabla q\prime} \, dV dt}_{J_{advh_{hf}}} \\
\text{where} \\
X\prime = X - \bar{X}
\end{cases}
\tag{10}
$$

The low-frequency horizontal PV-advection ($J_{advh_{lf}}$) was computed from the 30 day filtered low-frequency (denoted by overbars) components of current and PV. The high-frequency PV-advection was obtained by subtracting the low-frequency advection ($J_{advh_{lf}}$) from the total horizontal advection (J_{advh}) (see equation (10)).

Figures 13a and 13b indicate similar intensities of the high-frequency $J_{advh_{hf}}$ and low-frequency $J_{advh_{lf}}$ components in the total advection J_{advh}. This points out a high activity of the fine-scale structures in the horizontal transport because the term $J_{advh_{hf}}$ represents cross-frontal exchanges of PV through mesoscale and submesoscale eddies. High positive PV-intrusions inwardly of the gyre by $J_{advh_{hf}}$ are particularly vigorous in the meandering Balearic Front because due to its strong mesoscale variability. In the Kuroshio current system, *Bishop* [2012] found that eddy PV-fluxes across the front lead to a modification of Subtropical Mode Water in the recirculation gyre. Consequently, it can be expected that the positive high-frequency transport $J_{advh_{hf}}$ increases the stratification and creates cyclonic eddies within the gyre by PV-conservation. The stratification inside the gyre may be modified by a nonlocal process and not by a local atmospheric forcing as in the Gulf-Stream [*Thomas and Marshall*, 2005]. Actually, it is difficult to know on what proportions the stratification and circulation are modified by PV-conversion.
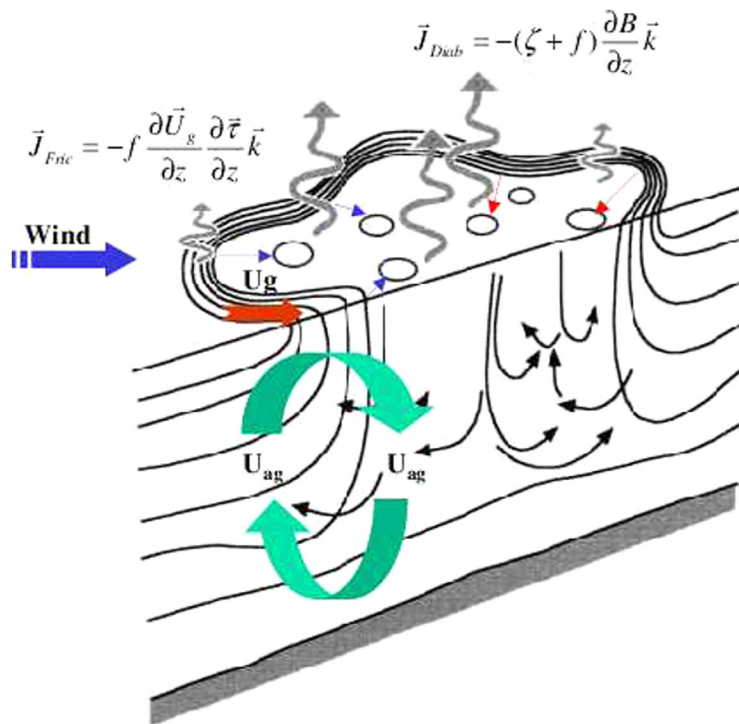
Figure 14. Conceptual scheme of destratification and dense water formation along the baroclinic cyclonic gyre in the North-Western Mediterranean Sea: (green arrows loop) The vertical cell and (downward black arrows) turbulence, and (U_g, red arrow) the geostrophic current act as a PV pump drawing high-PV from the pycnocline and the upstream region, respectively, to limit the frictional (J_{fric}) and diabatic (J_{diab}) PV-destruction at the surface. Horizontal arrows represent the eddy PV-fluxes which transport PV from the front inward the gyre. The basis of the Figure is taken from *Marshall and Schott* [1999].

The PV-budget was used to unravel the processes of the destratification mechanism in the baroclinic gyre. This destratification and subsequent dense water formation result from imbalance between the surface PV-destruction and subsurface PV-refueling as illustrated in Figure 14. The wind-front interactions represented by the frictional and diabatic PV-flux induce PV-destructions at the surface. The PV-destruction makes the front unstable and activates a cross-front ageostrophic cell which transports the near-surface (< 50 m) low-PV water downward and the subsurface (~ 150 m) high-PV water upward. The subsurface high-PV water is also upwelled by turbulence from the pycnocline. Also low-PV water tends to be laterally balanced by horizontal advection of the North Current.

In this way, the vertical cell, the turbulence, and the geostrophic current act as a PV

pump drawing high-PV water from the pycnocline and the upstream regions to limit the frictional and diabatic PV-destruction at the surface.

This scheme, primitively proposed by *Thomas* [2007] in a two-dimensional numerical study of a baroclinic zone, is confirmed and extended here to a real case of the western Mediterranean for dense water formation. Finally the frontal zone is connected with the mixed-patch through eddy PV-fluxes induced by instability of the gyre.

5. Energetics

In order to be compared with the air-sea buoyancy flux, *Thomas and Lee* [2005] rescaled the frictional PV-flux at the surface (second equation of system 8) into an equivalent wind driven buoyancy flux (their equation (15)) defined as follows:

$$EBF_{fric} = \frac{\rho C_p}{\alpha g} \vec{\tau}_0 \frac{\partial \vec{U}_g}{\partial z} \quad (\text{W m}^{-2})$$

where ρ, C_p, α, $\vec{\tau}_0$, and $\vec{U}_g$ are the surface water density, the specific heat, the thermal expansion coefficient, the surface wind-stress, and the geostrophic current, respectively. Because of the interaction between the strong lateral density gradient/strong vertical geostrophic shear $\left(\frac{\partial \vec{U}_g}{\partial z}\right)$ at fronts and surface wind stress in the large western boundary current systems, *Thomas and Lee* [2005] showed that EBF_{fric} ranges between 50 and 20000 W m^{-2} when using horizontal model resolutions between 400 and 1 km, respectively. This result points out that the wind-driven buoyancy flux can crush the atmospheric surface heat flux if the frontal zones are accurately resolved. The consequences in terms of mode water formation, their spread, and their impact on the general circulation may be important because coarse resolution models may lead to unrealistic PV destruction by wind.

In this study, an equivalent surface buoyancy flux (EBF_{diab}) is also derived for the diabatic PV-flux from the first equation of system (8) and is defined as follows:

$$EBF_{diab} = \frac{\rho C_p}{\alpha g} B_0 (1 + R_o) \quad (\text{W m}^{-2})$$

EBF_{diab} expresses the modulation of the surface buoyancy flux B_0 by the Rossby number $R_o = \frac{\zeta}{f}$, where ζ is the relative vorticity. Consequently, energy exchanges increase/decrease versus B_0 in presence of cyclonic/anticyclonic mesoscale and submesoscale structures. Somehow EBF_{diab} represents the coupling of the ocean vortical dynamics with the atmosphere.

The month-averaged sum of the diabatic and frictional PV-fluxes ($EBF = EBF_{diab} + EBF_{fric}$) presented in Figure 15a displays intensities down to -1400 W m^{-2}, that is 3.5 times stronger than the month-average surface buoyancy fluxes shown on Figure 2. On the other hand, note that patterns of EBF are captured in frontal and eddies regions, while those of the mean surface buoyancy flux mainly reflects the wind (Figure 2) and not the ocean structures evidenced by the density field.

The strongest negative intensities (-1400 W m^{-2}) of EBF along the northern branch of the North Current are mainly explained by the frictional component EBF_{fric} (Figure 15b) because of frequent northerly and downfront winds during February (Figure 2). The diabatic component EBF_{diab} (Figure 15c) destratifies the ocean (~ -400 W m^{-2}) mainly along the eastern branch of the North Current in the GL and the Ligurian Sea, and in the South part of the gyre. As shown in Figure 15b, the destratification is moderated by positive frictional fluxes ($EBF_{fric} \sim 200$ W m^{-2}). This corresponds to a PV input into the ocean by friction on account of opposed directions between the wind and current.

The EBF_{diab} increase versus B_0 (Figure 2) in frontal regions is linked to $R_o > 0$, while EBF_{diab} decreases toward B_0 inside of the gyre where $R_o \simeq 0$. These results highlight the time-integrated effects of the mesoscale and submesoscale density gradients and vorticity on surface energy exchanges. In that way, the surface PV-fluxes appear to be more representative of the ocean-atmosphere coupling in frontal mesoscale and submesoscale structures than air-sea fluxes.

The subsurface energy exchanges can also be estimated by deriving equivalent buoyancy fluxes for the Ekman layer. The diabatic and frictional EBF^{ek} are derived from the system (8) as follows:
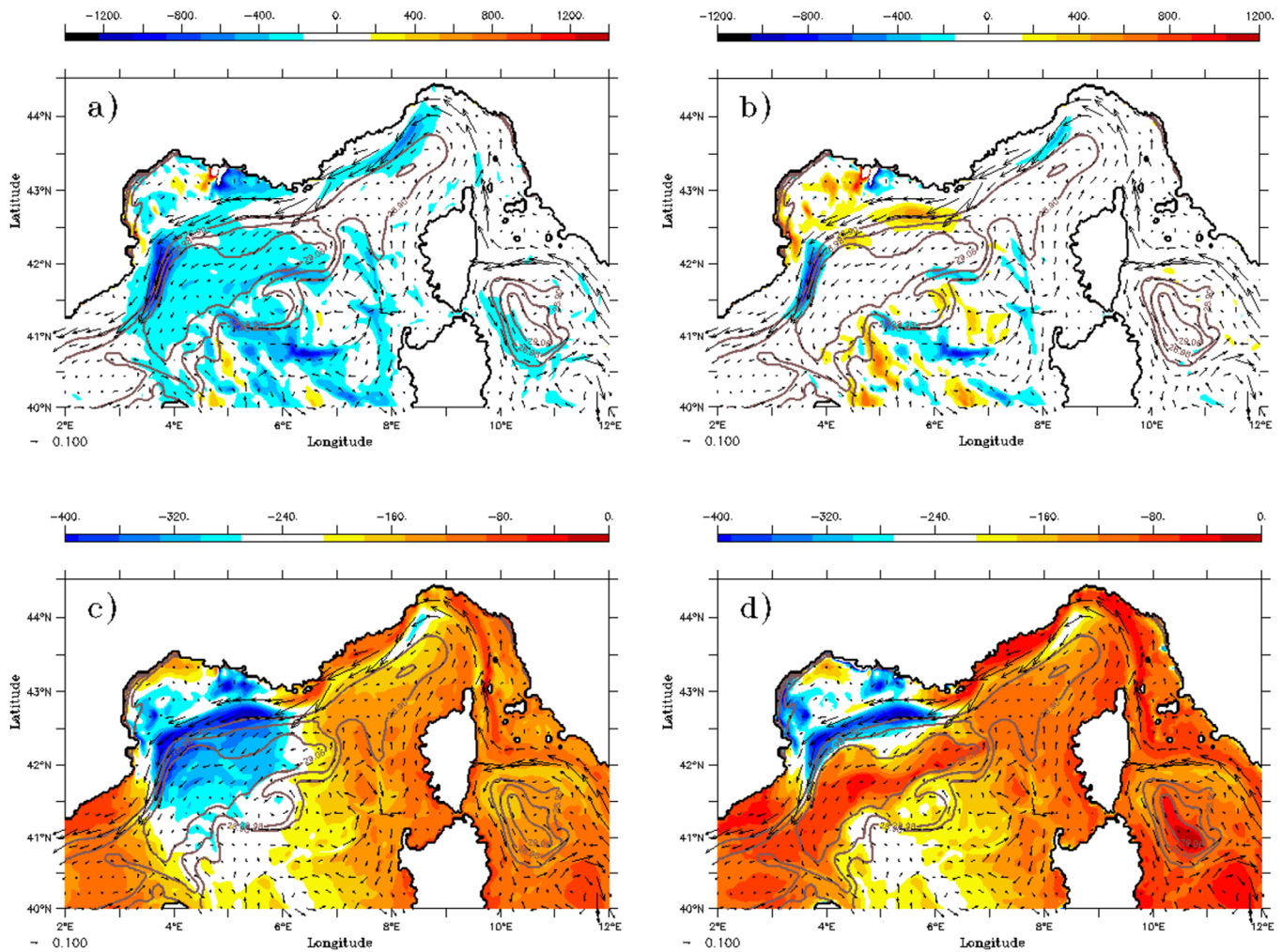
Figure 15. Surface equivalent buoyancy flux (W m^{-2}): (a) total, (b) frictional component, (c) diabatic component, and (d) Ekman diabatic component superimposed on the surface density (contour, kg m^{-3}) and current fields (arrows, m s^{-1}).

$$
\begin{cases}
EBF_{diab}^{ek} = \bar{\mathcal{J}}_{diab} \dfrac{\rho C_p}{\alpha f g} h_{ek} \\[2em]
EBF_{fric}^{ek} = \bar{\mathcal{J}}_{fric} \dfrac{\rho C_p}{\alpha f g} h_{ek}
\end{cases}
$$

where $\bar{\mathcal{J}}$ is the PV-flux averaged over the Ekman depth $h_{ek} = 0.4 \frac{u_*}{f}$. EBF^{ek} also includes the surface components.

The frictional component EBF_{fric}^{ek} is very close to the surface contribution EBF_{fric} because of sustained vertical shears of geostrophic current and stress in the Ekman layer (not shown). This is not the case for the diabatic terms at the surface EBF_{diab} (Figure 15c) and in the Ekman layer EBF_{diab}^{ek} (Figure 15d). Indeed EBF_{diab}^{ek} vanishes inside the cyclonic gyre but does not tend toward the atmospheric buoyancy flux B_0 as EBF_{diab}. This behavior is due to the deep mixed-layer depths at the center of the gyre which tend to collapse the B-divergence $\left(\frac{\partial B}{\partial z}\right)$ in the term $\bar{\mathcal{J}}_{diab}$. However thanks to sustained subsurface diabatic PV-destructions ($\bar{\mathcal{J}}_{diab} < 0$), the term EBF_{diab}^{ek} remains strong in frontal areas.

On 24 February, the Mistral wind generates surface buoyancy flux down to -800 W m^{-2} while the frictional and diabatic EBF reaches -3500 W m^{-2} in frontal regions around the gyre, where the wind is optimally oriented downfront (not shown). In such favorable conditions, a cross-front Ekman circulation sets up and increase the front intensity by horizontal convergence of isopycnals. This leads to strong intensities of the frictional EBF which in turn forces a cross-front ageostrophic circulation. The dynamic response

of the ocean to the *EBF* forcing is illustrated by the month-average vertical velocity in the northern branch of the North Current (Figure 12). *w* is upward (downward) on the light (dense) side of the front, which is suspected to subduct the new dense water formed at the surface in the frontal zone. This pattern is consistent with the dipole of vertical velocity shown in 7 February (Figure 11) and confirms that the ageostrophic cell across the front is robust and in agreement with the dynamics obtained in an academic 2-D front [*Thomas and Marshall*, 2005] and in the subpolar front of the Japan Sea during a cold air outbreak [*Thomas*, 2007].

The eddying area of the Balearic front also displays strong intensities at submesoscale. Such intensities stress the need to resolve accurately the fine scales of the ocean.

6. Conclusions

The North-Western Mediterranean Sea is prone to be subjected to important surface buoyancy losses which trigger deep convection in the GL in winter [*Herrmann and Somot*, 2008]. However if the surface energetic loss is an important ingredient for convection, *Béranger et al*. [2010] showed that the direction of Mistral and Tramontane winds relative to the gyre is the most important element for convection. A buoyancy loss, even limited, but well localized over the gyre intensifies the cyclonic circulation by geostrophic adjustment that maintains the waters under strong destratification.

These studies indicate that mode water formation and convection in the mixed-patch have long been treated as a buoyancy flux problem, especially in the Mediterranean, however the mechanisms at work along the baroclinic rim of the gyre were little investigated and poorly understood mainly in real cases. This study proposes to adopt a PV-perspective rather than the usual surface flux approach to identify all the processes of dense water formation at fronts during February 2013 of the HyMeX experiment.

The PV-budget is diagnosed from an ocean realistic simulation performed with the regional eddy-resolving (1/36°) model NEMO-WMED36, driven in surface by the hourly air-sea fluxes from the AROME-WMED forecasts atmospheric model (2.5 km resolution).

The simulated dense water formed in the density class $\sigma > 29.0 \text{ kg m}^{-3}$ during February 2013 were effectively produced along the rim of the cyclonic gyre where the North Current and density gradients are strong. The dense waters are well collocated with the PV-destruction associated with the surface frictional and buoyancy PV-fluxes. This suggests that surface PV destructions by momentum and buoyancy fluxes are sources of destratification and are relevant forcings of dense water formation.

Along the northern branch of the North Current, PV-destruction mainly results from the coupling between the friction and lateral buoyancy gradient. In this area, the bathymetry stabilizes the front and maintains the current northerly, which is thus persistently in the same direction as the dominant northerly wind. This configuration leads to optimal wind-current interactions and explains the frictional preponderance on the diabatic PV-destruction. This mechanical forcing set up a cross-front ageostrophic circulation, which subducts surface and subsurface low-PV waters destroyed by wind into interior and obducts high-PV waters from the pycnocline toward the surface. The horizontal PV-advections associated with the geostrophic North Current and turbulent entrainment at the pycnocline also contribute to the PV-refueling in frontal region. Finally, eddies formed by baroclinic instability are expulsed from the cyclonic gyre and transport mostly high PV water from the frontal region toward the center of the gyre. The net impact of this transport contributes to restratify the convection area. To conclude, the destratification and dense water formation result from the imbalance between the surface PV-destruction and subsurface PV-refueling. This mechanism of dense water formation in the baroclinic zone of the cyclonic gyre is a central result of this study and is illustrated by the conceptual scheme presented in Figure 14.

The energy involved in the interactions between the wind and the frontal mesoscale structures is evaluated by building equivalent buoyancy fluxes (*EBF*) from surface diabatic and frictional PV-fluxes. With -1400 W m^{-2}, the February average *EBF* at front is 3.5 times stronger than the surface buoyancy fluxes. During Mistral and Tramontane strong flux events, *EBF* decreases down to -3500 W m^{-2}, that is of the same order of magnitude as intensities found in the Gulf Stream [*Thomas and Marshall*, 2005] and the Japan Sea front during cold-air outbreak [*Thomas and Lee*, 2005]. If the diabatic *EBF* is everywhere negative and controls the ocean destratification in the North-Western basin because of strong cold and dry

air advections, the frictional *EBF* is positive meaning a restratification of the ocean in the south part of the gyre. However, Mistral and Tramontane winds are systematically downfront along the northern branch of the North Current that induces the most intense destratification by friction. Finally diabatic and frictional *EBF* are coupled ocean-atmosphere processes which involve huge energetic exchanges at the surface providing that the submesoscale oceanic features are accurately resolved. This points out the need to use appropriate horizontal resolutions to resolve *EBF* which can be view as energy trapping in fronts and eddies. This raises the question of the parameterization of these processes in climate models.

The ultimate goal is to estimate the volume flux of dense water formed from the surface nonadvective PV-fluxes. In principle, this is possible since according to the impermeability theorem [*Haynes and McIntre*, 1987], the PV fluxes through the isopycnal sheet 29.0 kg m^{-3} do not contribute to the PV budget on the volume ($\mathcal{V}$). As there is no diapycnal mixing, *Marshall and Nurser* [1992] propose to compute the formation of dense water from the surface PV-fluxes only. The volume of fluid subducted per unit of area is given by their equation (32) which can be rewritten here with our notations as follows:

$$DWF(\sigma > 29) = \sum_t -\frac{J_{flux}\Delta S}{\Delta q}\Delta t \tag{11}$$

where J_{flux} is the nonadvective PV-flux, ΔS is the section of the outcropping isopycnal layer $\sigma > 29.0$ kg m^{-3} and Δq is the PV change at the pycnocline. The interest of this approach would be to identify the diabatic and frictional contributions and to reveal the role of submesoscales in mode water formation. Theoretically, this method should be a suited metric to derive dense water formation; nevertheless it is difficult to implement it in real cases because of the difficulty to estimate accurately Δq. In fact Δq can be very small ($\sim 1 \times 10^{-10}$ s^{-3}), especially for a well-mixed ocean down to the bottom as the western Mediterranean, making estimates of dense water produced highly sensitive to errors of this parameter. A future work will be to derive an alternative relation more reliable than equation (11).

References

Badin, G., R. Williams, and J. Sharples (2010), Water-mass transformation in the shelf seas, *J. Mar. Res.*, *68*, 189–214.

Barnier, B., et al. (2006), Impact of partial steps and momentum advection schemes in a global ocean circulation model at eddy-permitting resolution, *Ocean Dyn.*, *56*(5-6), 543–567, doi:10.1007/s10,236–006–0082–1.

Béranger, K., Y. Drillet, M.-N. Houssais, P. Testor, R. Bourdallé-Badie, B. Alhammoud, A. Bozec, L. Mortier, P. Bouruet-Aubertot, and M. Crépon (2010), Impact of the spatial distribution of the atmospheric forcing on water mass formation in the Mediterranean Sea, *J. Geophys. Res.*, *115*, C12041, doi:10.1029/2009JC005648.

Beuvier, J., F. Sevault, M. Herrmann, H. Kontoyiannis, W. Ludwig, M. Rixen, E. Stanev, K. Béranger, and S. Somot (2010), Modelling the Mediterranean Sea interannual variability during 1961-2000: Focus on the Eastern Mediterranean Transient (EMT), *J. Geophys. Res.*, *115*, C08517, doi:10.1029/2009JC005950.

Beuvier, J., K. Béranger, C. L. Brossier, S. Somot, F. Sevault, Y. Drillet, R. Bourdallé-Badie, N. Ferry, B. Levier, and F. Lyard (2012), Spreading of the western Mediterranean deep water after winter 2005: Time-scales and deep cyclone transport, *J. Geophys. Res.*, *117*, C07022, doi:10.1029/2011JC007,679.

Bishop, S. (2012), The role of eddy fluxes in the Kuroshio Extension at 144°−148°e, PhD thesis, Univ. of Rhode Island, Kingston. [Available at http://digitalcommons.uri.edu/dissertations/AAI3524054.]

Blanke, B., and P. Delecluse (1993), Low frequency variability of the tropical ocean simulated by a general circulation model with mixed layer physics, *J. Phys. Oceanogr.*, *23*, 1363–1388.

Chelton, D., R. deSzoeke, M. Schlax, K. E. Naggar, and N. Siwertz (1998), Geographical variability of the first baroclinic Rossby radius of deformation, *J. Phys. Oceanogr.*, *28*, 433–460.

Drobinski, P., et al. (2014), HyMeX, a 10-year multidisciplinary program on the Mediterranean water cycle., *Bull. Am. Meteorol. Soc.*, *95*, 1063–1082, doi:10.1175/BAMS-D-12-00242.1.

Ducrocq, V., et al. (2014), HyMeX-SOP1, the field campaign dedicated to heavy precipitation and flash flooding in the northwestern Mediterranean., *Bull. Am. Meteorol. Soc.*, *95*, 1083–1100, doi:10.1175/BAMS-D-12-00244.1.

Estournel, C., et al. (2016), HyMeX-SOP2, the field campaign dedicated to dense water formation in the northwestern mediterranean, *Oceanography*, *29*(4), 196–206. [Available at https://doi.org/10.5670/oceanog.2016.94.]

Foltz, G., S. A. Grodsky, J. A., Carton, and M. J. McPhaden (2003), Seasonal mixed layer heat budget of the tropical {A}tlantic Ocean, *JGR*, *108*(C5), 3146, doi:10.1029/2002JC001584/

Forget, G., G. Maze, M. Buckley, and J. Marshall (2011), Estimated seasonal cycle of north Atlantic eighteen degree water volume, *J. Phys. Oceanogr.*, *41*(2), 269–286.

Fourrié, N., et al. (2015), AROME-WMED, a real-time mesoscale model designed for HyMeX special observation periods, *Geosci. Model Dev.*, *8*, 1919–1941, doi:10.5194/gmd-8-1919-2015.

Gascard, J. (1978), Mediterranean deep water formation, baroclinic instability and oceanic eddies, *Oceanol. Acta*, *1*, 315–330.

Gaspar, P., Y. Grégoris, and J. Lefevre (1990), A simple eddy kinetic energy model for simulations of the oceanic vertical mixing: Tests at station papa and long-term upper ocean study site, *J. Geophys. Res.*, *95*, 16,179–16,193.

Giordani, H., L. Prieur, and G. Caniaux (2006), Advanced insights into sources of vertical velocity in the ocean, *Ocean Dyn.*, *56*(5), 513–524, doi:10.1007/s10,236-005-0050-1.

Giordani, H., G. Caniaux, and A. Voldoire (2013), Intraseasonal Mixed-Layer Heat Budget in the Equatorial Atlantic during the Cold Tongue development in 2006, *J. Geophys. Res. Oceans*, *118*, 650–671, doi:10.1029/2012JC008280.

Hamad, N., C. Millot, and I. Taupier-Letage (2005), A new hypothesis about the surface circulation in the eastern basin of the Mediterranean Sea, *Prog. Oceanogr.*, *66*, 287–298.

Haynes, P., and M. McIntre (1987), On the evolution of vorticity and potential vorticity in the presence of diabatic heating and frictional or other forces, *J. Atmos. Sci.*, *44*, 828–841.

Herrmann, M., and S. Somot (2008), Relevance of ERA40 dynamical downscaling for modeling deep convection in the Mediterranean Sea, *Geophys. Res. Lett.*, *35*, L04607, doi:10.1029/2007GL032442.

Herrmann, M., C. Estournel, M. Déqué, P. Marsaleix, F. Sevault, and S. Somot (2008a), Dense water formation in the Gulf of Lions shelf: Impact of atmospheric interannual variability and climate change, *Cont. Shelf Res.*, *28*(15), 2092–2112, doi:10.1016/j.csr.2008.03.003.

Herrmann, M., S. Somot, F. Sevault, C. Estournel, and M. Déqué (2008b), Modeling the deep convection in the northwestern Mediterranean Sea using an eddy-permitting and an eddy-resolving model: Case study of winter 1986-1987, *J. Geophys. Res.*, *113*, C04011, doi:10.1029/2006JC003991.

Hoskins, B., M. McIntyre, and A. Robertson (1985), On the use and significance of isentropic potential vorticity maps, *Q. J. R. Meteorol. Soc.*, *111*, 877–946.

Houpert, L., et al. (2016), Observations of open-ocean deep convection in the North-Western Mediterranean Sea: Seasonal and interannual variability of mixing and deep water masses for the 2007-2013 period, *J. Geophys. Res. Oceans*, *121*, doi:10.1002/2016JC011857, in press.

Klein, P., G. Lapeyre, and W. Large (2004), Wind ringing of the ocean in presence of mesoscale eddies, *Geophys. Res. Lett.*, *31*, L15306, doi:10.1029/2004GL020274.

Lascaratos, A., W. Roether, K. Nittis, and B. Klein (1999), Recent changes in deep water formation and spreading in the Eastern Mediterranean Sea, *Prog. Oceanogr.*, *44*, 5–36.

Latif, M., and T. Barnett (1994), Causes of decadal climate variability over the North Pacific and North America, *Science*, *266*, 634–637, doi:10.1126/science.266.5185.634.

Lazar, A., G. Madec, and P. Delecluse (1999), The deep interior downwelling in the Veronis effect, and mesoscale tracer transport parameterizations in an OGCM, *J. Phys. Oceanogr.*, *29*, 2945–2961.

Lebeaupin-Brossier, C., and P. Drobinski (2009), Numerical high-resolution air-sea coupling over the Gulf of Lions during two Tramontane/mistral events, *J. Geophys. Res.*, *114*, D10110, doi:10.1029/2008JD011601.

Lebeaupin-Brossier, C., T. Arsouze, K. Béranger, M.-N. Bouin, E. Bresson, V. Ducrocq, H. Giordani, M. Nuret, R. Rainaud, and I. Taupier-Letage (2014), Ocean Mixed Layer Responses to intense meteorological events during HyMeX-SOP1 from a high-resolution ocean simulation, *Ocean Modell.*, *84*, 84–103, doi:10.1016/j.ocemod.2014.09.009.

Léger, F., C. L. Brossier, H. Giordani, T. Arsouze, J. Beuvier, M. Bouin, E. Bresson, V. Ducrocq, N. Fourrié, and M. Nuret (2016), Dense Water Formation in the North-Western Mediterranean area during HyMeX-SOP2 in 1/36° ocean simulation: Sensitivity to initial conditions, *J. Geophys. Res. Oceans*, *121*, 5549–5569, doi:10.1002/2015JC011542.

Lellouche, J., et al. (2013), Evaluation of global monitoring and forecasting systems at Mercator Océan, *Ocean Sci.*, *9*, 57–81, doi:10.594/os-9-57-2013.

L'Hévéder, B., L. Li, F. Sevault, and S. Somot (2013), Interannual variability of deep convection in the Northwestern Mediterranean simulated with a coupled AORCM, *Clim. Dyn.*, *41*, 937–960, doi:10.1007/s00382-012-1527-5.

Lyard, F., F. Lefèvre, T. Letellier, and O. Francis (2006), Modelling the global ocean tides: Modern insights from FES2004, *Ocean Dyn.*, *56*(5–6), 394–415.

Madec, G. (2008), NEMO Ocean Egine, *Note du Pôle de Modélisation*, vol. 27, technical report 1288-1619, LOCEAN, Inst. Pierre Simon Laplace (ipsl), Univ. P. et M. Curie, Paris, France.

Madec, G., M. Chartier, P. Delecluse, and M. Crépon (1991), A three-dimensional numerical studies of deep-water formation in the Northwestern Mediterranean Sea, *J. Phys. Oceanogr.*, *21*, 1349–1371.

Madec, G., F. Lott, P. Delecluse, and M. Crépon (1996), Large-scale preconditioning of deep-water formation in the northwestern Mediterranean Sea, *J. Phys. Oceanogr.*, *26*, 1393–1408, doi:10.1175/1520-0485(1996)026.

Mahadevan, A., and A. Tandon (2006), An analysis of mechanisms for submesoscale vertical motion at ocean fronts, *Ocean Modell.*, *14*, 241–256.

Marshall, D., and F. Schott (1999), Open-ocean convection: Observations, Theory, and Models, *Rev. Geophys.*, *37*, 1–64.

Marshall, J., and A. Nurser (1992), Fluid dynamics of oceanic thermocline ventilation, *J. Phys. Oceanogr.*, *22*, 583–595.

Maze, G., and J. Marshall (2011), Diagnosing the observed seasonal cycle of Atlantic subtropical mode water using potential vorticity and its attendant theorems, *J. Phys. Oceanogr.*, *41*, 1986–1999.

Millot, C. (1999), Circulation in the western Mediterranean sea, *J. Mar. Syst.*, *20*(14), 423–442.

Orlanski, I. (1976), A simple boundary condition for unbounded hyperbolic flows, *J. Comput. Phys.*, *21*, 251–269.

Pasquet, A., T. Szekely, and Y. Morel (2012), Production and dispersion of mixed waters in stratified Costal areas, *Cont. Shelf Res.*, *39*, 49–77.

Peter, C., M. Le Hénaff, Y. du Penhoat, C. E. Menkés, F. Marin Jérome Vialard, G. Caniaux, A. Lazar (2006), A model study of the seasonal mixed-layer heat budget in the equatorial Atlantic, *JGR*, *111*, C06014, doi:10.1029/2005JC003157.

Rainville, L., S. Jayne, J. McClean, and M. Maltrud (2007), Formation of subtropical mode water in a high-resolution simulation of the Kuroshio extension region, *Ocean Modell.*, *17*(4), 338–356, doi:10.1016/j.ocemod.2007.03.002.

Reynolds, R., T. Smith, C. Liu, D. Chelton, K. Casey, and M. Schlax (2007), Daily high-resolution-blended analyses for sea surface temperature, *J. Clim.*, *20*, 5473–5496, doi:10.1175/2007JCLI1824.1.

Roulet, G., and G. Madec (2000), Salt conservation, free surface and varying levels: A new formulation for ocean general circulation models, *J. Geophys. Res.*, *105*, 23,927–23,942, doi:10.1029/2000JC900089.

Schott, F., M. Visbec, U. Send, J. Fischer, L. Stramma, and Y. Desaubies (1996), Observations of deep convection in the Gulf of Lion, Northern Mediterranean, during the winter of 1991/1992, *J. Phys. Oceanogr.*, *26*, 505–524.

Small, R., S. Carniel, T. Campbell, J. Teixeira, and R. Allard (2012), The response of the Ligurian and Tyrrhenian Seas to a summer Mistral event: A coupled atmosphere-ocean approach, *Ocean Modell.*, *48*, 30–44.

Speer, K., and E. Tziperman (1992), Rate of Water Mass Formation in the North Atlantic Ocean, *J. Phys. Oceanogr.*, *22*, 93–104.

Speer, K., E. Guilyardi, and G. Madec (2000), Southern Ocean transformation in a coupled model with and without eddy mass fluxes, *Tellus Ser. A*, *52*, 554–565.

Thomas, L. (2007), Dynamical constraints on the extreme low values of the potential vorticity in the ocean, in *Extreme events: Aha Hulikoa Hawaiian Winter Workshop, University of Hawaii at Manoa, January 23-26, 2007*, Sch. of Ocean and Earth Sci. and Technol., Honolulu, Hawaii.

Thomas, L. (2008), Formation of intrathermocline eddies at ocean fronts by wind-driven destruction of potential vorticity, *Dyn. Atmos. Oceans*, *38*, 252–273.

Thomas, L., and R. Ferrari (2008), Friction, frontogenesis, and the stratification of the surface mixed-layer, *J. Phys. Oceanogr.*, *38*, 2501–2518.

Thomas, L. N., and C. M. Lee (2005), Intensification of ocean fronts by down-front winds, *J. Phys. Oceanogr.*, *35*, 1086–1102.

Thomas, L. N., and J. Marshall (2005), CLIMODE, in *Destruction of Potential Vorticity by Winds: Implications for the Formation of Eighteen Degree Water, CLIMODE Meeting*. [Available at http://www.climode.org/Meetings/SEP_05.]

Tziperman, E. (1986), On the role of interior mixing and air-sea fluxes in determining the stratification and circulation of the oceans, *J. Phys. Oceanogr.*, *16*, 680–693.

Waldman, R., et al. (2016), Estimating dense water volume and its evolution for the year 2012-2013 in the North-western Mediterranean Sea: An observing system simulation experiment approach, *J. Geophys. Res. Oceans*, *121*, 6696–6716, doi:10.1029/2016JC011694.

Walin, G. (1982), On the relation between sea-surface heat flow and the thermal circulation in the ocean, *Tellus*, *34*, 187–195.